

## INFLUENCE OF POROSITY AND PORE DENSITY ON THE THERMAL AND HYDRAULIC PERFORMANCE OF METAL FOAM HEAT EXCHANGERS

Huisseune H.\*, De Schampheleire S., Ameel B. and De Paepe M.

\*Author for correspondence

Department of Flow, Heat and Combustion Mechanics,

Ghent University,

Sint-Pietersnieuwstraat 41

9000 Gent

Belgium

E-mail: [henkhuisseune@ugent.be](mailto:henkhuisseune@ugent.be)

### ABSTRACT

Metal foam shows a great potential for heat transfer applications. In this work the influence of the volumetric porosity, the pore density and the foam material (aluminum or copper) on the heat transfer and pressure drop characteristics are investigated. Two-dimensional simulations are performed using a porous medium approach: the Darcy-Forchheimer-Brinkman flow model is combined with the two-equation energy model. Round tube heat exchanger with a staggered tube layout are considered. Simulations are performed for inlet velocities between 1.2 m/s and 3.2 m/s.

The validation experiment shows a good match between the simulations and the measurements, proving the quality of the simulations. It is found that the friction factor is mainly determined by the porosity, while the Colburn j-factor is mainly determined by the pore density. For a given pumping power the heat exchanger volume increases with decreasing PPI value to perform the same heat duty. For the same PPI value and a fixed pumping power, the heat exchanger volume increases with increasing porosity. For the same fan power, the heat transfer rate for copper foam is up to 20% higher compared to foam made of the aluminum alloy AlSi7Mg0.3. Comparison to a bare tube bundle shows that the heat transfer rate of a foamed heat exchanger is up to 6 times larger for the same fan power. This article illustrates that optimization is required to design heat exchangers which fully benefit from the unique advantages of open-cell metal foam.

### INTRODUCTION

In many applications heat is transferred with air. The main thermal resistance is then located at the air-side. To increase the heat transfer rate, the air-side heat transfer surface is enlarged by adding fins. Today many different fin types and fin topologies exist (e.g. louvers, slits, vortex generators, etc.).

Improving the fin designs becomes thus more and more difficult. Instead of improving existing fin designs, the heat transfer rate at the air-side can also be increased by using new materials. Such a material which shows large potential for thermal applications is open-cell metal foam. This porous material consists of a network of solid ligaments around the pores. This is illustrated in Figure 1. Open-cell metal foams are characterized by a high porosity (and thus low weight), a high surface-to-volume ratio and excellent fluid mixing. Together with the high thermal conductivity of aluminum or copper these foams are a promising structure for heat transfer applications.

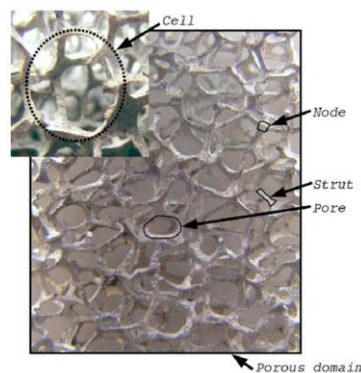


**Figure 1** Open-cell metal foam with introduction of some terminology

Metal foams can be treated as porous media. Due to time constraints, microscopic analysis of metal foam is usually restricted to a limited number of cells [1]. A macroscopic analysis is possible using the volume averaging technique (VAT). In VAT models the details of the original structure are replaced by their averaged counterparts. The governing VAT transport equations were previously developed from the mass, momentum and energy equations by Whitaker [2] and Travnin

and Catton [3], see Eqs. (1)-(4). The second term on the right-hand side of Eq. (2) is called the Brinkman term, the third term is the Darcy term and the last term is the Forchheimer term. Two energy equations are considered (Eqs. (3)-(4)), which means that thermal non-equilibrium is assumed between the fluid and solid phase. This assumption is necessary due to the large difference in thermal conductivity between the fluid and the foam material. These equations for the phase averaged variables can be solved much faster than the traditional transport equations for local variables, which require direct numerical simulations (DNS). However, because the details of momentum and energy transfer between the fluid flow and solid structure are lost during the averaging, closure relations are required. These include relations for the interstitial heat transfer coefficient  $h_{sf}$ , the permeability  $\kappa$  and the inertial loss factor  $\beta$  [4-10]. Effective properties, such as effective thermal conductivity  $k_{fe}$  and  $k_{se}$  (fluid and solid, resp.) and effective viscosity  $\mu_{fe}$ , are also introduced [8-11].

$$\nabla \cdot \vec{v} = 0 \quad (1)$$

$$\frac{\rho_f \vec{v} \cdot \nabla \vec{v}}{\phi} = -\phi \nabla P + \mu_f^e \nabla^2 \vec{v} - \frac{\mu_f \vec{v}}{\kappa} - \rho_f \beta \|\vec{v}\| \vec{v} \quad (2)$$

$$(\rho c_p)_f \vec{v} \cdot \nabla T_f = \nabla \cdot k_f^e \nabla T_f - A_{sf} h_{sf} (T_f - T_s) \quad (3)$$

$$0 = \nabla \cdot k_s^e \nabla T_s - A_{sf} h_{sf} (T_s - T_f) \quad (4)$$

At the Ghent University a macroscopic model which allows simulating the thermal hydraulic performance of open-cell metal foams is developed based on the volume averaging technique (VAT) [12]. This model combines the Darcy-Forchheimer-Brinkman flow model with a thermal non-equilibrium energy model, as described by Eqs. (1)-(4). The closure relations and effective properties were derived for open-cell metal foam with high porosity ( $\phi > 88\%$ ). These foams are most suitable for heat transfer applications due to their open structure.

De Schampheleire et al. [13] tested a 10PPI metal foam heat exchanger with round tubes in a wind tunnel. The measurement data will be used here to validate the developed VAT model. Next, the validated model will be used to study the influence of the porosity, pore density and foam material on the thermal hydraulic performance of this heat exchanger.

## NOMENCLATURE

$A_c$	[m <sup>2</sup> ]	minimum cross sectional flow area
$A_i^*$	[-]	relative heat exchanger frontal area (Eq. (18))
$A_o$	[m <sup>2</sup> ]	overall heat transfer surface area
$C_{min}$	[W/K]	minimum heat capacity
$c_p$	[J/kgK]	specific heat capacity
$d_{c1}$	[m]	small cell diameter
$d_{c2}$	[m]	large cell diameter
$D_h$	[m]	hydraulic diameter
$D_o$	[m]	outer tube diameter

$d_s$	[m]	strut diameter
$f$	[-]	fanning friction factor
$F_d$	[m]	heat exchanger flow depth
$G_c$	[kg/m <sup>2</sup> s]	mass flux through the minimum cross section
$h$	[W/m <sup>2</sup> K]	convective heat transfer coefficient
$H$	[m]	heat exchanger height
$j$	[-]	Colburn j-factor
$k$	[W/mK]	thermal conductivity
$\dot{m}$	[kg/s]	mass flow rate
$NTU$	[-]	number of transfer units
$P$	[Pa]	pressure
$P_d^*$	[-]	relative fluid pumping power (Eq. (20))
$P_l$	[m]	longitudinal tube pitch
$Pr$	[-]	Prandtl number
$P_t$	[m]	transversal tube pitch
$Q$	[W]	heat transfer rate
$R$	[K/W]	thermal resistance
$Re$	[-]	Reynolds number
$T$	[K]	temperature
$t_w$	[m]	tube wall thickness
$U$	[W/m <sup>2</sup> K]	overall heat transfer coefficient
$v$	[m/s]	superficial velocity
$V_d^*$	[-]	relative heat exchanger volume (Eq. (19))
$W$	[m]	heat exchanger width

### Special characters

$\beta$	[m <sup>-1</sup> ]	inertial loss factor
$\varepsilon$	[-]	effectiveness
$\phi$	[-]	porosity
$\eta_o$	[-]	surface efficiency
$\kappa$	[m <sup>2</sup> ]	permeability
$\mu$	[Pas]	dynamic viscosity
$\rho$	[kg/m <sup>3</sup> ]	density
$\sigma$	[-]	contraction ratio
$\sigma_o$	[m <sup>2</sup> /m <sup>3</sup> ]	specific surface area

### Subscripts and superscripts

$e$	effective
$f$	fluid
$in$	inlet
$m$	mean
$out$	outlet
$s$	solid
$sf$	interstitial

## COMPUTATIONAL DOMAIN AND PROCEDURE

Figure 2 shows the computational domain which corresponds to the heat exchanger geometry tested by Deschampsheleire et al. [13]. The large width of the actual heat exchanger justifies the use of two-dimensional simulations. The heat exchanger consists of two tube rows placed in a staggered tube layout. Each tube row counts 10 tubes. The geometrical details are listed in Table 1. The computational domain is divided in four zones: the pre-extended region, the post-extended region, the porous zone and the tube walls. The pre-extended region equals 1.25 times the flow depth of the heat exchanger, while the post-extended region measures 4 times the flow depth of the heat exchanger. The porous zone is a metal foam block with a height equal to 256 mm and a flow depth of 24 mm. The tube walls were also meshed to take the heat conduction into account. The quality of the mesh was carefully assessed during the meshing. All zones were meshed with quadrilateral elements. In the porous zone a mesh size of 0.20 mm is used. In the pre- and post-extended region a growth

function is applied with a growth rate 1.08 and 1.05, respectively. The mesh counts 181000 cells. The grid independency was verified by reducing the mesh size. The heat transfer and pressure drop results of the finest mesh (cell size = 0.10 mm in porous zone; total number of cells = 630000) only differed 1.5% and 0.3%, respectively, compared to the coarser mesh. Due to this small differences and taking into account the computational time, the mesh counting 181000 is used for the simulations throughout this paper.

To investigate the influence of the porosity and pore density nine different metal foams were investigated. Their characteristics are listed in Table 2. Each foam sample is assigned an ID number: MFxx.yyy with xx the PPI value (pores per linear inch; also referred to as pore density) and yyy the specific surface area. Both are macroscopic geometric parameters. The relation between microscopic and macroscopic parameters is reported by De Jaeger et al. [14]. MF10.462 corresponds to the metal foam which was previously tested in the wind tunnel [13]. As the metal foam cells are elliptic, two cell diameters are reported ( $d_{c1}$  and  $d_{c2}$ ).  $d_s$  represents the strut diameter. A practical lower limit for the strut diameter is 0.1 mm, because thinner struts are too fragile.  $\phi$  is the volumetric porosity (defined as the ratio of the air volume to the total volume) and  $\sigma_o$  is the specific surface area.

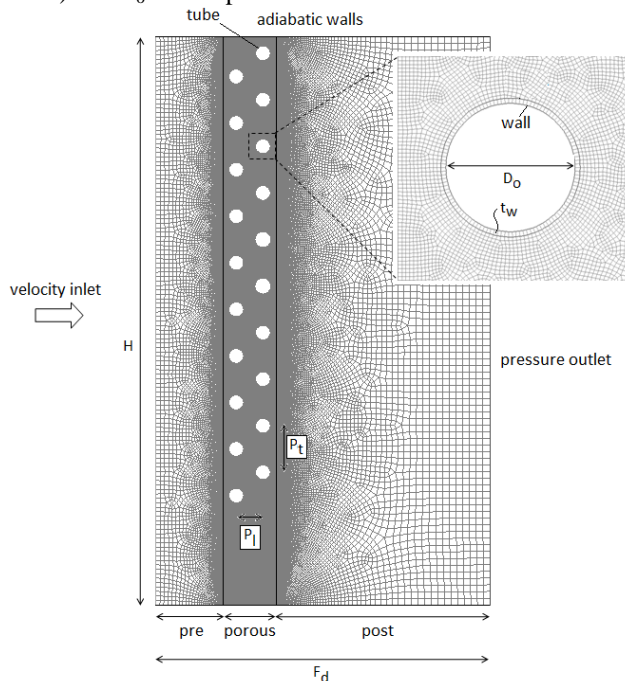


**Figure 2** Two-dimensional computational domain

**Table 1** Geometrical details of the metal foam heat exchanger

Parameter	Symbol	Unit	Value
Heat exchanger height	H	mm	256
Heat exchanger width	W	mm	426
Heat exchanger depth	$F_d$	mm	24
Tube outer diameter	$D_o$	mm	7.2
Tube wall thickness	$t_w$	mm	0.27
Transversal tube pitch	$P_t$	mm	21
Longitudinal tube pitch	$P_1$	mm	12

**Table 2** Foam parameters of the studied aluminum foam

ID	PPI	$d_{c1}$ (mm)	$d_{c2}$ (mm)	$d_s$ (mm)	$\phi$	$\sigma_o$ ( $m^2/m^3$ )
MF10.380	10	4.28	6.42	0.28	0.951	380
MF10.462	10	4.22	6.23	0.36	0.932	462
MF20.580	20	2.60	3.67	0.13	0.967	580
MF20.720	20	2.77	4.15	0.22	0.937	720
MF20.860	20	2.52	3.78	0.24	0.913	860
MF30.1310	30	1.67	2.50	0.16	0.914	1310
MF35.1515	35	1.45	2.17	0.14	0.913	1515
MF40.1767	40	1.23	1.84	0.12	0.907	1767
MF45.2080	45	1.05	1.58	0.10	0.903	2080

At the inlet of the computational domain a uniform velocity (1.2 m/s – 3.2m/s) in the x-direction and a constant air inlet temperature (21.0°C – 24.1°C) were imposed. The inlet velocities and inlet temperatures were the same as during the measurements by De Schampheleire et al. [13]. At the outlet the static pressure was set to 0 Pa (pressure outlet boundary condition). The walls of the flow channel are considered adiabatic (i.e. well insulated during the experiment). The tube wall with a thickness of 0.27 mm was meshed. A convective heat transfer coefficient and free stream temperature were applied on the inner wall of the tubes. The free stream temperature is the same as the bulk water temperature measured during the experiments (62.8°C- 65.5°C), while the convective heat transfer coefficient is equal to the one determined during the experiments using the Gnielinski correlation [15] (4758W/m<sup>2</sup>K – 4865 W/m<sup>2</sup>K). The heat exchanger previously tested in the wind tunnel has two dummy tubes in the second tube row through which no water flowed (i.e. it is a so called ‘low capacity unit’, meaning that not all tubes are connected to the headers) [13]. The inner surfaces of these two tubes are modeled as adiabatic walls. No slip boundary conditions were applied on the tube outer walls. The contact resistance between the tubes and foam is modeled as an extra thermal resistance resulting in a temperature jump at the foam/tube interface. The value for this contact resistance is taken from De Jaeger et al. [16]. The double precision pressure based solver was used. The coupled algorithm was applied for the pressure-velocity coupling. The discretization of the convective terms in the governing equations is done via a second order upwind scheme, while a second order central differencing scheme is applied for the diffusive terms. The gradients are evaluated via the least squares cell based method. The pressure gradient in the momentum equations is treated via a second order discretization scheme. Convergence criteria were set to 10<sup>-6</sup> for continuity and velocity components and 10<sup>-10</sup> for energy. Setting smaller values for these criteria did not result in any notable differences in the flow field and heat transfer predictions. The air density was calculated as for an incompressible ideal gas and the air specific heat was calculated via a polynomial fit. The molecular viscosity was determined via the Sutherland approximation. The molecular thermal conductivity was determined based on the kinetic theory. The density, specific heat and thermal conductivity of the metal foam materials were considered constant (for

aluminum AL1050:  $\rho = 2710 \text{ kg/m}^3$ ,  $c_p = 871 \text{ J/kgK}$  and  $k_s = 220 \text{ W/mK}$ ; for copper C10100:  $\rho = 8960 \text{ kg/m}^3$ ,  $c_p = 380 \text{ J/kgK}$  and  $k_s = 390 \text{ W/mK}$ ). Also the copper tubes have constant material properties. For each of the simulations the resulting heat balance closes within 0.2% and there were no noticeable differences in the mass balance.

## EXPERIMENTAL VALIDATION

The measurements performed by Deschampeleire et al. [13] are used here to validate the simulation results. The aluminum foam MF10.462 is connected to the tubes via a pressure fitting. The heat exchanger was experimentally characterized for six different air mass flow rates, resulting in inlet velocities ranging from 1.2 m/s to 3.2 m/s. Comparison of the measurements with the VAT predictions allows evaluating the accurateness of the VAT model. During the wind tunnel measurements the tubes were heated with hot water. Hence, a temperature gradient exists at the waterside. The simulations on the other hand are two-dimensional assuming a fixed free stream water temperature. Calculating the total heat transfer of the simulated heat exchanger by multiplying the computed heat transfer (in W/m) with the heat exchanger width results in the overall heat transfer for a fixed fluid temperature in the tubes. Hence, to make a fair comparison between the measurements and the simulations, the experimental data were recalculated to the situation with fixed water temperature. De Schampeleire et al. [13] determined the overall heat transfer resistance from the heat transfer measurements using the effectiveness-NTU relation for a mixed/unmixed configuration. The resulting overall heat transfer resistance was then recalculated to the heat transfer using the effectiveness-NTU relation for zero heat capacity ratio according to Eq. (5). This is the special case for constant fluid temperature at one side of the heat exchanger, corresponding to our simulations.

$$\varepsilon = 1 - \exp(-NTU) \quad (5)$$

Figure 3 plots the heat transfer and pressure drop results. The uncertainty bars on the experimental data are also indicated. The maximum deviation in heat transfer is 3%, while the pressure drop predictions fall within the experimental uncertainty of the measurements. This good match between experiments and simulations validates the VAT model.

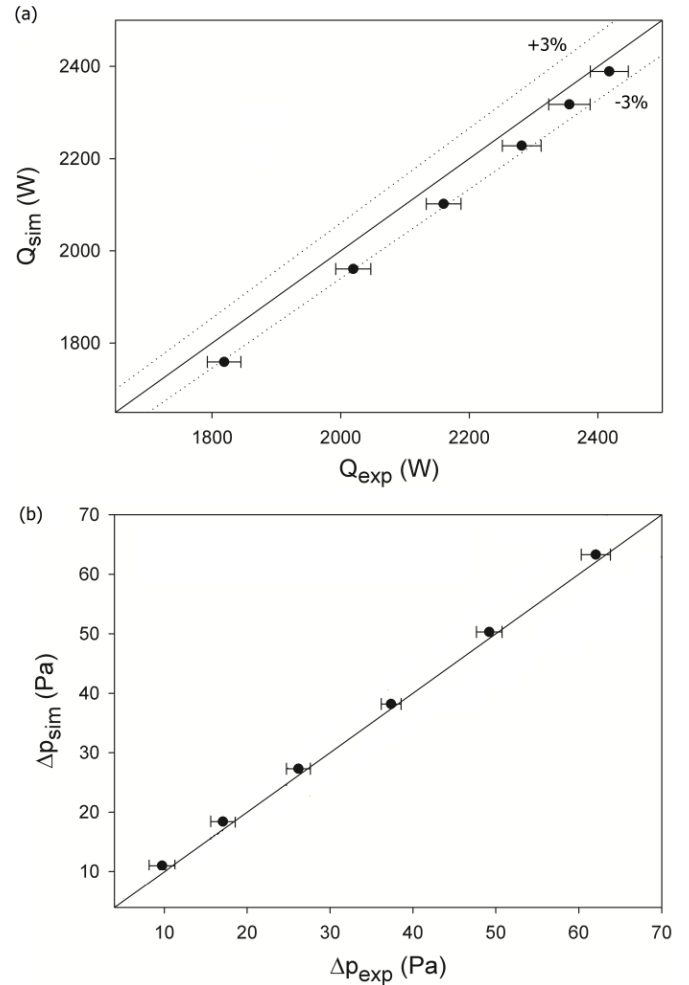


Figure 3 Experimental validation of the VAT model

## DATA REDUCTION METHOD

The Reynolds number is based on the hydraulic diameter  $D_h$  and the velocity  $V_c$  in the minimum cross sectional flow area, see Eq. (6).

$$Re_{D_h} = \frac{\rho_{air} V_c D_h}{\mu_{air}} \quad (6)$$

The hydraulic diameter  $D_h$  is calculated as in [17-18]:

$$D_h = \frac{4A_c F_d}{A_o} \quad (7)$$

with  $A_c$  the minimum cross sectional flow area,  $F_d$  the heat exchanger depth and  $A_o$  the total heat transfer surface area at the air-side. The contraction ratio  $\sigma$ , defined as the ratio of the minimum cross sectional area  $A_c$  to the frontal heat exchanger area, is calculated according to Eq. (8). Here  $\phi$  is the foam porosity,  $P_t$  is the transversal tube pitch and  $D_o$  is the exterior tube diameter. The maximum velocity  $V_c$  is then determined from Eq. (9).

$$\sigma = \phi \frac{P_t - D_o}{P_t} \quad (8)$$

$$V_c = \frac{V_{front}}{\sigma} \quad (9)$$

The pressure drop is expressed dimensionless as a fanning friction factor  $f$  using Eq. (10) [18,20-21]. In this equation  $G_c$  is the mass flux in the minimum cross sectional flow area  $A_c$  (Eq. (11)) and  $\rho_m$  is the mean density between inlet and outlet. The friction factor includes the entrance and exit pressure loss.

$$f = \frac{A_c \rho_m}{A_o \rho_{in}} \left( \frac{2 \rho_{in} \Delta P}{G_c^2} - (1 + \sigma^2) \left( \frac{\rho_{in}}{\rho_{out}} - 1 \right) \right) \quad (10)$$

$$G_c = \rho_m V_c \quad (11)$$

The heat transfer results are reported dimensionlessly as Colburn  $j$ -factors. These were calculated from the VAT simulation results using the  $\varepsilon$ -NTU method. The effectiveness  $\varepsilon$  is determined as

$$\varepsilon = \frac{Q}{C_{min} \cdot (T_{tube} - T_{air,in})} \quad (12)$$

with  $Q$  the total heat transfer rate,  $C_{min}$  the air-side heat capacity ( $\dot{m} \cdot c_p$ ) and  $T_{tube}$  and  $T_{air,in}$  the free stream tube temperature and the air inlet temperature applied in the 2D simulations, respectively. The NTU is then calculated from Eq. (5). The overall heat transfer resistance  $(UA)^{-1}$  can then be determined from Eq. (13).

$$\frac{1}{UA} = \frac{1}{C_{min} \cdot NTU} \quad (13)$$

The overall heat transfer resistance consists of four parts: the convective resistance  $R_i$  at the tube side, the conductive resistance  $R_{cond}$  through the tube material, the contact resistance  $R_{contact}$  at the tube-foam/air interface and the convective resistance  $R_o$  at the air-side. This results in Eqs. (14)-(15) from which the air-side convective resistance  $R_o$  can be calculated.

$$R_{contact} = \left( \frac{1}{R_{contact,foam}} + \frac{1}{R_{contact,air}} \right)^{-1} \quad (14)$$

$$\frac{1}{UA} = R_i + R_{cond} + R_{contact} + R_o \quad (15)$$

The air-side convective heat transfer coefficient  $h_o$  is then given by:

$$\eta_o \cdot h_o = \frac{1}{A_o \cdot R_o} \quad (16)$$

The surface efficiency  $\eta_o$  takes the effect of a finite foam thermal conductivity into account. Notice that the surface efficiency is not separated from the convective heat transfer

coefficients. They are presented as one entity because the surface efficiency and the convective heat transfer coefficient clearly form one component of the total heat transfer resistance. The convective heat transfer coefficients are reported dimensionless as Colburn  $j$ -factors (including the surface efficiency) according to Eq. (17).

$$j = \frac{\eta_o h_o}{\rho V_c c_p} Pr^{2/3} \quad (17)$$

From a thermal hydraulic point of view, heat exchanger design is always a trade-off between heat transfer, which should be as large as possible, and fan power, which should be as small as possible. Cowell [19] introduced several methods to compare compact heat transfer surfaces. He showed that for a given number of transfer units NTU, mass flow rate and inlet fluid temperature (and thus a given heat transfer rate) the relative values defined by Eqs. (18)-(20) are directly proportional to the heat exchanger frontal area, the total heat exchanger volume and fluid pumping power, respectively. They will be used to develop dimensionless performance plots which allow comparing the performance of different heat exchangers.

$$A_d^* = \frac{D_h}{\sigma Re \varepsilon D_h} \quad [m] \quad (18)$$

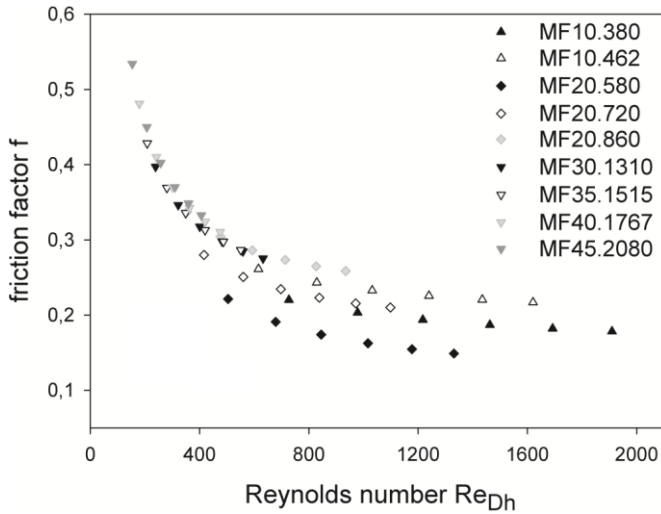
$$V_d^* = \frac{D_h^2}{\sigma j Re \varepsilon D_h} \quad [m^2] \quad (19)$$

$$P_d^* = \frac{f Re^2 D_h^2}{j D_h^2} \quad [m^{-2}] \quad (20)$$

## RESULTS AND DISCUSSION

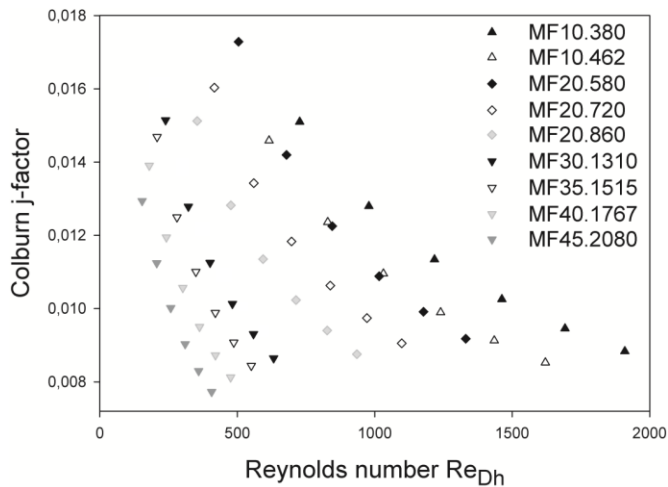
### Influenc of the porosity and pore density

Figure 4 shows that the friction factor increases with decreasing porosity. The smallest friction factor is found for MF20.580 which has a porosity of 96.7%, while the largest friction factor is found for MF45.2080 having a porosity of 90.3%. Notice that the foams MF20.860, MF30.1310 and MF35.1515 have the same porosity (about 91.3%), which explains why they coincide. This is not surprising, because – referring to Eq. (2) – the pressure drop across the heat exchanger is mainly determined by the Forchheimer contribution. For  $Re_{ds} > 20$  (Reynolds number based on the strut diameter and the superficial velocity), De Schamphelre et al. [19] showed that the contribution of the Forchheimer term to the pressure gradient is much larger than the contribution of the Darcy term. The Reynolds range of Figure 4 corresponds to  $20 < Re_{ds} < 125$ . The contribution of the Brinkman term and the term on the left-hand side in Eq. (2) is also very small. The latter even equals zero in case of a fully developed flow. The inertial loss factor  $\beta$  in the Forchheimer term is modeled as function of the porosity [12], which explains the strong link between friction factor and porosity.



**Figure 4** Friction factors for the different foams

Figure 5 shows the Colburn j-factors as function of the Reynolds number. It can be concluded that the Colburn j-factors increase with reducing PPI value. For a given PPI value, the largest Colburn j-factors are found for the foam with largest porosity (e.g. compare the three 20 PPI samples: MF20.580 has a porosity  $\phi = 96.7\%$ , MF20.720 has a porosity  $\phi = 93.7\%$  and MF 20.860 has a porosity  $\phi = 91.3\%$ ).



**Figure 5** Colburn j-factors for the different foams

In Figure 6 the relative pumping power  $P_d^*$  is plotted against the relative volume  $V_d^*$  for the nine metal foam heat exchangers at constant heat transfer. To the right of each curve the hydraulic diameter  $D_h$  is indicated. On each curve six symbols are presented which correspond to the values of the relative frontal area  $A_d^*$  marked on curve MF45.2080. For a given pumping power  $P_d^*$  the heat exchanger volume  $V_d^*$  increases with decreasing PPI value to perform the same heat duty. For  $P_d^* = 16.6 \times 10^{11} \text{ m}^{-2}$ , for instance, the heat exchanger volume of the 10PPI foam MF10.380 is about  $3.8/1.0 = 3.8$  times larger than the volume of the 45PPI foam MF45.2080, while the heat exchanger volume of the 20PPI foam MF20.720 is only  $2.1/1.0 = 2.1$  times larger. Further notice that the 45PPI

heat exchanger has the largest frontal area (i.e.  $A_d^* = 8.3 \times 10^{-6} \text{ m}^2$ ). The 20PPI heat exchanger has a frontal area which is 29% ( $= (8.3-5.9)/8.3$ ) smaller than the frontal area of the 45PPI heat exchanger, while the 10PPI heat exchanger has a frontal area which is even 34% smaller ( $= (8.3-5.5)/8.3$ ). For the same PPI value and a fixed pumping power  $P_d^*$ , the heat exchanger volume  $V_d^*$  increases with increasing porosity. Consider for instance the two 10PPI heat exchangers: at a given pumping power  $P_d^* = 16.6 \times 10^{11} \text{ m}^{-2}$ , the volume of MF10.380 is 12% larger than the volume of MF10.462 ( $= (3.8 - 3.4)/3.4$ ). When comparing the 45PPI heat exchanger with the 30PPI heat exchanger it can be seen that for the same total volume (e.g.  $V_d^* = 1.35 \times 10^{-6} \text{ m}^2$ ) the frontal area of the 45PPI foam is double ( $= 13.8/6.9$ ) of the frontal area of the 30PPI foam to perform the same heat duty. A larger frontal area for a given volume means that the 45PPI foam has a shorter flow depth which results in a smaller pressure drop. Indeed, the pumping power when using the 45PPI foam is about  $17.4/6.1 = 2.9$  times lower compared to the 30PPI foam.

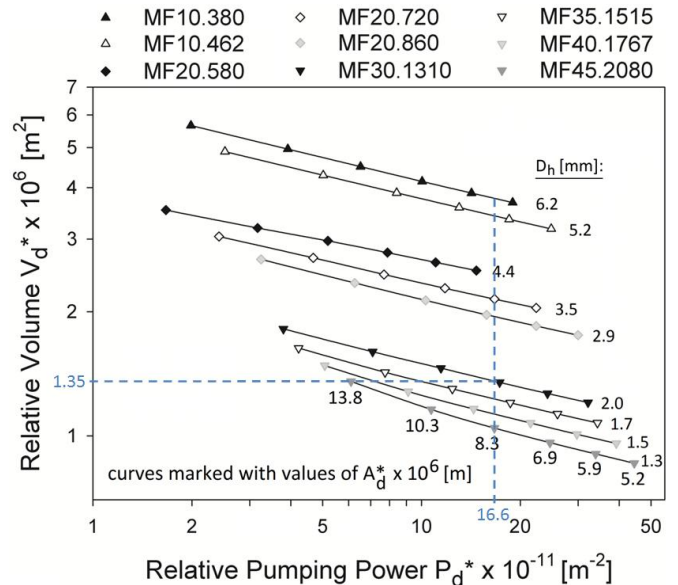


**Figure 6** Relative volume plotted as function of the relative pumping power for metal foam heat exchangers at constant heat transfer (given number of transfer units and mass flow rate)

### Influence of the foam material

In conventional finned heat exchangers, a higher thermal conductivity of the fin material results in a better heat transfer. This is quantified with the fin efficiency [20]. Similarly, a higher thermal conductivity of the foam material will also result in a better thermal performance. To assess the influence of the foam material three different simulations are performed for metal foam MF45.2080. Two aluminum types are evaluated: AlSi7Mg0.3 with a conductivity of 150 W/mK and pure aluminum (i.e. Al1050) with a conductivity of 220 W/mK. Also copper foam, with a thermal conductivity of 390 W/mK is simulated (i.e. copper C10100). These materials are frequently used to produce open-cell metal foams for thermal applications. In Figure 7 the heat transfer rate is plotted for the heat exchanger geometry of Figure 2. The simulations were

performed for foam MF45.2080. A higher thermal conductivity clearly is beneficial for heat transfer. In the considered mass flow rate range the heat transfer of Al1050 is 6 to 8% higher compared to AlSi7Mg0.3. The copper foam C10100 even has a heat transfer rate which is 12 to 20% higher compared to AlSi7Mg0.3. Compared to Al1050, copper C10100 shows between 6% to 10% increase in heat transfer rate. Even though AlSi7Mg0.3 is used in many thermal applications, Al1050 and C10100 foams are clearly outperforming them. As is known, copper is more expensive than aluminum (per unit of volume). However, the price of metal foam is mainly determined by the production process and less by the material cost. As the production process (i.e. casting a PU preform) is for both materials quite similar, the additional cost per unit of volume copper foam is limited. Moreover, due to the increased thermal performance, the required volume copper foam is smaller than the required volume aluminum foam for the same heat duty. It is thus important that for every thermal application the choice of foam material is well considered, based on a thermo economic analysis.

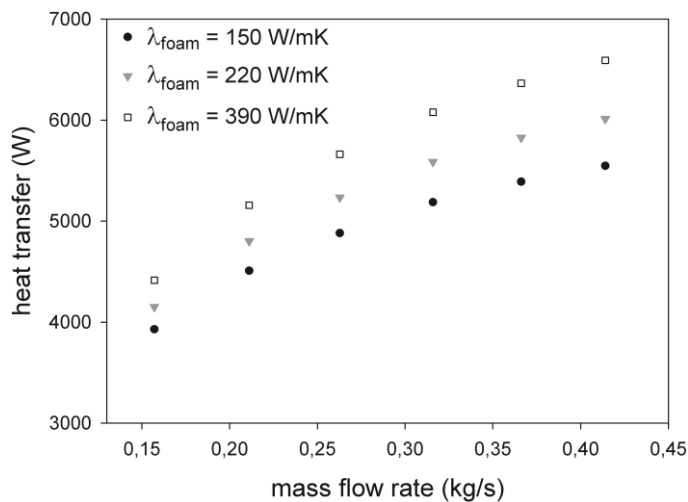


**Figure 7** Heat transfer rate for three different foam materials (AlSi7Mg0.3, Al1050 and C10100) of foam MF45.2080.

### Comparison to a bare tube bundle

Figure 8 shows the heat transfer rate as function of the fan power. The fan power is calculated as the product of the pressure drop over the heat exchanger and the volumetric flow rate at the heat exchanger inlet. The nine metal foam heat exchangers made of Al1050 are shown, as well as the 45PPI heat exchanger made of C10100. As a reference, also a bare tube bundle is plotted having the same staggered tube layout as the metal foam heat exchangers. The heat transfer and fan power of the bare tube bundle are calculated using the Nusselt and Euler correlations of Zukauskas for a staggered tube bundle [21]. For the same fan power and overall dimensions, the heat transfer rate clearly increases with the specific surface area. All metal foam heat exchangers outperform the bare tube bundle. The copper 45PPI heat exchanger shows a 6 times higher heat transfer than the bare tube bundle at the same fan power.

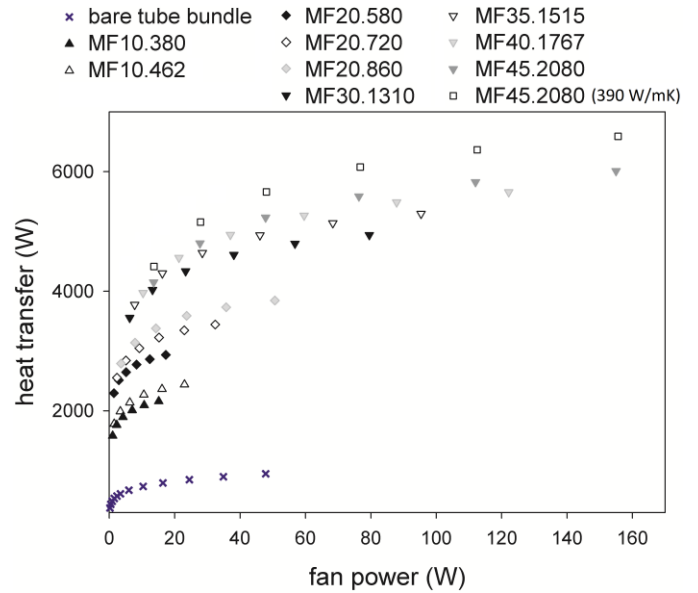


**Figure 8** Heat transfer rate as function of fan power for the different metal foam heat exchangers and a bare tube bundle

## CONCLUSIONS

In this work the Darcy-Forchheimer-Brinkman flow model combined with the two-equation energy model (thermal non-equilibrium) is used to simulate the thermal and hydraulic performance of metal foam heat exchangers. Round tube heat exchangers having a staggered tube layout are considered. The effect of the porosity and the pore density of nine different metal foams is investigated as well as the influence of the foam material. The experimental validation proves the accurateness of the simulation results.

Compared to a bare tube bundle with the same tube layout as the foamed heat exchangers, the heat transfer rate when using foam is up to 6 times larger for the same fan power. Further, it is found that the friction factors are mainly determined by the porosity, while the Colburn  $j$ -factors are determined by the pore density: the friction factors increase with reducing porosity, while the Colburn  $j$ -factors increase with reducing pore density. The dimensionless performance plot shows that for a given pumping power the heat exchanger volume decreases with increasing PPI value to perform the same heat duty. For the same PPI value and a fixed pumping power, the heat exchanger volume increases with increasing porosity. The foam material also strongly affects the thermal performance. This clearly indicates that the heat exchanger performance is strongly dependent on many parameters (dimensions, velocities, foam material, etc.). Consequently, optimization is required to obtain high performance metal foam heat exchangers which fully benefit from the unique advantages of open-cell metal foam.

## REFERENCES

- [1] Boomsma K., Poulikakos D., and Zwick F. Metal foams as compact high performance heat exchangers, *Mechanics of Materials*, Vol. 35, 2003, pp. 1161–1176.
- [2] Whitaker S., The method of volume averaging, Kluwer Academic, Boston, 1999.
- [3] Travkin V.S., and Catton I. Transport phenomena in heterogeneous media based on volume averaging theory, *Advances in Heat Transfer*, G.G. Hari and A.H. Charles, ed. Elsevier, 2001, pp. 1-144.
- [4] Nakayama A., Ando K., Yang C., Sano Y., Kuwahara F., and Liu J. A study on interstitial heat transfer in consolidated and unconsolidated porous media, *Heat Mass Transfer*, Vol. 45, 2009, pp. 1365-1372.
- [5] Teruel F.E., and Díaz L. Calculation of the interfacial heat transfer coefficient in porous media employing numerical simulations, *International Journal of Heat and Mass Transfer*, Vol. 60, 2013, pp. 406-412.
- [6] Madani B., Topin F., Rigollet F., and Tadrist L. Flow laws in metallic foams: Experimental determination of inertial and viscous contributions, *Journal of Porous Media*, Vol. 10, No. 1, 2007, pp. 51-70.
- [7] Dukhan N., and Minjeur C.A. A two-permeability approach for assessing flow properties in metal foam, *Journal of Porous Materials*, Vol. 18, 2011, pp. 417-424.
- [8] Calmidi V.V., and Mahajan R.L. Forced convection in high porosity metal foams, *Journal of Heat Transfer*, Vol. 122, 2000, pp. 557-565.
- [9] Bhattacharya A., Calmidi V.V., and Mahajan R.L. Thermophysical properties of high porosity metal foams, *International Journal of Heat and Mass Transfer*, Vol. 45, 2002, pp. 1017-1031.
- [10] Magnico P. Analysis of permeability and effective viscosity by CFD on isotropic and anisotropic metallic foams, *Chemical Engineering Science*, Vol. 64, 2009, pp. 3564-3575.
- [11] Wang M. and Pan N. Modeling and prediction of the effective thermal conductivity of random open-cell porous foams, *International Journal of Heat and Mass Transfer*, Vol. 51, 2008, pp. 1325-1331.
- [12] De Jaeger P., T'Joel C., Huisseune H., Ameel B., De Schampheleire S., and De Paepe M. Influence of geometrical parameters of open-cell aluminum foam on thermo-hydraulic performance, *Heat Transfer Engineering*, Vol. 34, No. 14, 2013, pp. 1202-1215.
- [13] De Schampheleire S., De Jaeger P., Huisseune H., Ameel B., T'Joel C., De Kerpel K., and De Paepe M. Thermal hydraulic performance of 10 PPI aluminium foam as alternative for louvered fins in a HVAC heat exchanger, *Applied Thermal Engineering*, Vol. 51, No. 1-2, 2013, pp. 371-382.
- [14] De Jaeger P., T'Joel C., Huisseune H., Ameel B., and De Paepe M. An experimentally validated and parameterized periodic unit-cell reconstruction of open-cell foams, *Journal of Applied Physics*, Vol. 109, no. 103519 (10 pages), 2011.
- [15] Gnielinski V. New Equations for Heat and Mass Transfer in Turbulent Tube and Channel Flow, *International Chemical Engineering*, Vol. 29, 1976, pp. 359-368.
- [16] De Jaeger P., T'Joel C., Huisseune H., Ameel B., and De Paepe M. Assessing the influence of four bonding methods on the thermal contact resistance of open-cell aluminum foam, *International Journal of Heat and Mass Transfer*, Vol. 55, No. 21-22, 2012, pp. 6200-6210.
- [17] Wang C.C., Lee C.J., Chang C.T., Lin S.P. Heat transfer and friction correlation for compact louvered fin-and-tube heat exchangers, *International Journal of Heat and Mass Transfer*, Vol. 42, No. 11, 1999, pp. 1945-1956.
- [18] Ameel B., Degroote J., T'Joel C., De Jaeger P., Huisseune H., De Schampheleire S., Vierendeels J., and De Paepe M. Optimization of X-shaped louvered fin and tube heat exchangers with respect to a physical performance criterion, *Applied Thermal Engineering*, Vol. 58, No. 1-2, 2013, pp. 136-145.
- [19] Cowell T.A. A general method for the comparison of compact heat transfer surfaces, *Journal of Heat Transfer - Transactions of the ASME*, Vol. 112, 1990, pp. 288-294.
- [20] R.K. Shah, D.P. Sekulic, Fundamentals of Heat Exchanger Design, John Wiley & Sons, Inc., Hoboken, New Jersey, 2003.
- [21] Zukauskas A. Heat transfer from tubes in cross flow, in *Handbook of single phase convective heat transfer*, Wiley Interscience, 1987.